The Astrophysical Journal, 734:40 (11pp), 2011 June 10 doi:10.1088/0004-637X/734/1/40
© 2011. The American Astronomical Society. All rights reserved. Printed in the U.S.A.

THE MID-INFRARED LUMINOSITY FUNCTION AT $z < 0.3$ FROM 5MUSES: UNDERSTANDING THE STAR FORMATION/ACTIVE GALACTIC NUCLEUS BALANCE FROM A SPECTROSCOPIC VIEW

Yanling Wu[1], Yong Shi[1], George Helou[1], Lee Armus[2], Daniel A. Dale[3], Casey Papovich[4], Nurur Rahman[5], Kalliopi Dasyra[6], and Sabrina Stierwalt[2]

[1] Infrared Processing and Analysis Center, California Institute of Technology, 1200 East California Boulevard, Pasadena, CA 91125, USA; yanling@ipac.caltech.edu, yong@ipac.caltech.edu, gxh@ipac.caltech.edu

[2] Spitzer Science Center, California Institute of Technology, 1200 East California Boulevard, Pasadena, CA 91125, USA; lee@ipac.caltech.edu, sabrina@ipac.caltech.edu

[3] Department of Physics & Astronomy, University of Wyoming, WY, USA; ddale@uwyo.edu

[4] George P. and Cynthia Woods Mitchell Institute for Fundamental Physics and Astronomy, Department of Physics and Astronomy, Texas A&M University, College Station, TX 77843-4242, USA; papovich@physics.tamu.edu

[5] Department of Astronomy, University of Maryland, College Park, MD 20742, USA; nurur@astro.umd.edu

[6] Irfu/Service d' Astrophysique, CEA Saclay, France; kalliopi.dasyra@obspm.fr

Received 2010 December 7; accepted 2011 April 1; published 2011 May 24

ABSTRACT

We present rest-frame 15 and 24 μm luminosity functions (LFs) and the corresponding star-forming LFs at $z < 0.3$ derived from the 5MUSES sample. Spectroscopic redshifts have been obtained for ∼98% of the objects and the median redshift is ∼0.12. The 5–35 μm Infrared Spectrograph spectra allow us to estimate accurately the luminosities and build the LFs. Using a combination of starburst and quasar templates, we quantify the star formation (SF) and active galactic nucleus (AGN) contributions in the mid-IR spectral energy distribution. We then compute the SF LFs at 15 and 24 μm, and compare with the total 15 and 24 μm LFs. When we remove the contribution of AGNs, the bright end of the LF exhibits a strong decline, consistent with the exponential cutoff of a Schechter function. Integrating the differential LF, we find that the fractional contribution by SF to the energy density is 58% at 15 μm and 78% at 24 μm, while it goes up to ∼86% when we extrapolate our mid-IR results to the total IR luminosity density. We confirm that the AGNs play more important roles energetically at high luminosities. Finally, we compare our results with work at $z \sim 0.7$ and confirm that evolution on both luminosity and density is required to explain the difference in the LFs at different redshifts.

Key words: galaxies: active – galaxies: luminosity function, mass function – galaxies: starburst – infrared: galaxies

Online-only material: color figures

1. INTRODUCTION

The unprecedented sensitivity of the *Spitzer Space Telescope* (Werner et al. 2004) has opened a new window to explore the infrared (IR) universe. IR luminous galaxies, discovered from ground-based (Rieke & Low 1972) and space (Soifer et al. 1987) observations, constitute an important population. While ultraluminous infrared galaxies (ULIRGs; $L_{\rm IR} > 10^{12}\,L_{\odot}$) only account for ∼5% of the IR luminosity in the local universe, their contribution becomes increasingly important at higher redshift, e.g., luminous infrared galaxies (LIRGs; $10^{11}\,L_{\odot} < L_{\rm IR} < 10^{12}\,L_{\odot}$) are responsible for 70%±15% of the energy density at $z \sim 1$ (Le Floc'h et al. 2005) and ULIRGs may become equally important as LIRGs at $z \sim 2$.

Recent surveys with the Multiband Imaging Photometer for *Spitzer* (MIPS; Rieke et al. 2004), as well as earlier observations with the *Infrared Space Observatory* (*ISO*), probe the dust emission at much fainter levels than that has been reached by the *Infrared Astronomical Satellite* (*IRAS*). This has vastly improved our understanding of galaxy evolution. Surveys with *IRAS* first established the local benchmark for mid- and far-IR luminosity functions (LFs; Soifer et al. 1987; Saunders et al. 1990; Rush et al. 1993; Shupe et al. 1998; Sanders et al. 2003). In the 1990s, 15 μm ISOCAM observations were used to derive the 15 μm LF (Xu 2000) at low redshift, as well as to study the evolution effects from the number counts (Elbaz et al. 1999; Chary & Elbaz 2001). The recent work of Bothwell et al. (2011) has constrained the slope of the IR and UV LFs at the extreme faint end for the first time using large data sets of local galaxies, and has derived the distribution function of star formation (SF) rate in the local universe. Deep MIPS surveys carried out in the past few years fertilized the ground for understanding the evolution of LF. Le Floc'h et al. (2005) illustrated the variation of 15 μm LF in the range of $0.3 < z < 1.2$ and suggested that the comoving IR energy density evolves dramatically, increasing with look-back time as $(1+z)^{3.9\pm0.4}$ up to $z \sim 1$ (Caputi et al. 2007; Reddy et al. 2008; Magnelli et al. 2009).

IR bright galaxies emit the bulk of their energy as dust-reprocessed light generated by dusty SF or accretion onto the supermassive black holes, referred to hereafter as active galactic nuclei (AGNs). Obtaining information on the relative contribution of SF/AGN is critical for understanding a galaxy's integrated emission. Le Floc'h et al. (2005) explored the SF history at $0.3 < z < 1.2$. However, the MIPS 24 μm photometry they used for that study did not allow them to account for the AGN contribution, or constrain the relationship between the stellar mass growth and black hole mass growth. The recent work of Magnelli et al. (2009), Rujopakarn et al. (2010), Fu et al. (2010), and Goto et al. (2011) has identified AGN-dominated sources and excluded these objects from their samples to derive the SF LFs. The shape of the LF depends on the rest-frame wavelength. UV/optical LF usually follows the profile of a Schechter function (Arnouts et al. 2005; Ilbert et al. 2005), while at mid/far-IR wavelengths, the bright-end slope is observed to be shallower than the exponential cutoff of a Schechter function (Soifer et al. 1987; Rush et al. 1993; Sanders et al. 2003).

This is rather intriguing because both UV and far-IR emission traces the same SF, and the different shapes for the LFs are suggested to be a result of dust extinction effect. The recent work of Fu et al. (2010) claims that the shallower slope of the IR LF could be due to the contribution of AGN at the high-luminosity end and when the AGN component is removed, the SF LF can be fit with a Schechter function. This further motivates our work of separating the SF and AGN emission in our objects to understand their contribution to the LF.

To quantify the relative contribution of SF and AGNs to the infrared luminosities, spectral decompositions have been performed by several groups (Sajina et al. 2008; Pope et al. 2008; Murphy et al. 2009; Menéndez-Delmestre et al. 2009). In high mid-IR luminosity systems at $z \sim 2$, Sajina et al. (2008) found an average AGN fraction of ∼20%–30% of total IR luminosity for strong polycyclic aromatic hydrocarbon (PAH) sources while this number goes up to ⩾70% for weak-PAH sources. The study of Pope et al. (2008) of a sample of submillimeter galaxies at similar redshift has revealed at most a 30% contribution from AGNs at mid-IR (5–11.5 μm rest frame). In the local universe, the contribution of nuclear activity to the bolometric luminosity of ULIRGs has been quantified with six independent methods by Veilleux et al. (2009), reaching an average AGN contribution of ∼35%–40%, whereas Nardini et al. (2008) suggest that intense SF accounts for 85% of the IR emission in local ULIRGs, with AGNs contributing 15%. It is clear that the relative contribution of SF/AGN varies in galaxies of different luminosities (Yuan et al. 2010; Hopkins et al. 2010), with the AGN playing more critical roles in more luminous systems. It must also be a function of wavelength, since the spectral energy distribution (SED) of the two components is quite distinct. The different selection criteria and decomposition techniques among different samples and authors also add to the differences derived in the relative contributions of SF and AGNs.

Current studies on IR LFs are mostly based on MIPS 24 μm observations, which imply a heavy reliance on the SED library used to make *k*-corrections and derive the monochromatic continuum or total infrared luminosities. Recently, Fu et al. (2010) have derived 8 μm and 15 μm LFs, as well as the corresponding SF LF, for a sample of $z \sim 0.7$ objects, taking advantage of their Infrared Spectrograph (IRS) spectra (Houck et al. 2004). The 5 Millijansky Unbiased Extragalactic Survey (5MUSES), an infrared spectroscopic survey of 330 objects selected by their MIPS 24 μm flux densities, provides an important sample for understanding the infrared galaxy population (G. Helou et al. 2011, in preparation). Although IR LFs have been extensively studied at low redshift, we find 5MUSES to be a unique sample for deriving LF for the following reasons: (1) being a mid-IR flux-limited sample, we reach a wide range of infrared luminosity ($\sim 10^9\ L_\odot$ to $\sim 10^{12}\ L_\odot$). (2) We reach higher redshifts than previous samples, e.g., the Revised Bright Galaxy Sample (Sanders et al. 2003). (3) The IRS spectra of our sample and far-IR measurements for most of them allow us to minimize the uncertainties on *k*-correction and luminosity estimation associated with adopting specific SEDs to be applied to all sources. (4) Last but not the least, the IRS spectra allow for a careful decomposition of every single source into an SF and AGN component and estimation of their contribution to the luminosity density. This will facilitate further studies on how the SF/AGN fraction in the integrated luminosity density evolves in a cosmological context.

The paper is organized as follows. In Section 2, we briefly describe the sample selection, and then the infrared and optical data used in this study. We introduce our methodology of using the $1/V_{\rm max}$ method to derive LF in Section 3, where we also demonstrate how we correct for the incompleteness of the 5MUSES sample. In the same section, we discuss in detail our methods of the SF/AGN decomposition of the IRS spectra and how we estimate the SF contribution in a statistical sense. The 15 and 24 μm LFs, as well as the corresponding SF LFs, are presented in Section 4, together with a discussion of how the SF fraction varies with luminosity and wavelength. We summarize our conclusions in Section 5. Throughout this paper, we assume a ΛCDM cosmology with $H_0 = 70$ km s^{-1}, $\Omega_m = 0.27$, and $\Omega_\lambda = 0.73$.

2. OBSERVATION AND DATA REDUCTION

2.1. The Sample

5MUSES is a mid-infrared spectroscopic survey of 330 galaxies with 24 μm flux densities 5 mJy $< f_\nu$ (24 μm) $<$ 100 mJy. The sources are selected from the SWIRE (Elais-N1, Elais-N2, Lockman Hole, and *XMM*) and the Extragalactic First Look Survey (XFLS) fields, covering a total area of 40.6 deg^2 on the sky. It provides a representative sample at intermediate redshift ($\langle z \rangle = 0.144$), previously unexplored by *Spitzer* since most of the spectroscopic work was focused on nearby spiral galaxies (SINGS; Kennicutt et al. 2003), local LIRGs, and ULIRGs (Armus et al. 2007, 2009; Veilleux et al. 2009), and the much fainter and more distant ($z \sim 2$) galaxies (Houck et al. 2005; Yan et al. 2007). A total of 1111 objects have f_ν(24 μm) between 5 and 100 mJy from the five survey fields of 5MUSES excluding stars. In order to efficiently observe the objects using the staring mode of IRS and include the largest fraction of a galaxy's integrated light, only objects unresolved within an aperture of $d = 10\farcs5$ (corresponding approximately to the slit width of the Long-Low module of IRS) are included in the final pool and this results in a total of 800 sources. Then 330 objects are randomly selected from the 800 final candidates. The details of the sample can be found by G. Helou et al. (2011, in preparation).

2.2. Data Reduction

We have obtained low-resolution mid-IR spectra for all 330 objects in 5MUSES using the Infrared Spectrograph on board the *Spitzer Space Telescope*. Both Short-Low (SL: 5.2–14.5 μm) and Long-Low (LL: 14–37 μm) modules are used, with spectral resolution of 64–128. The integration time on each object ranges from 300 to 960 s to achieve roughly the same signal-to-noise ratio (Wu et al. 2010). The IRS data are processed by the *Spitzer* Science Center data reduction pipeline version S17 and our data reduction starts from the pipeline products designated as "basic calibrated data (bcd)." The two-dimensional spectrograms are median combined and then the off-source sky regions are subtracted. After removing the sky background, the spectrograms are cleaned with the IRSCLEAN package to remove bad pixels and apply rogue pixel correction. Then the background-subtracted cleaned spectrograms are reduced with the optimal extraction method of the *Spitzer* IRS Custom Extractor (SPICE) software to extract the one-dimensional spectra. The details on the reduction of the IRS data can be found in Wu et al. (2010).

The IRS spectra allow us to derive redshifts for sources with mid-IR emission and/or absorption features. We have also searched for optical spectra of our sample in the literature. A total of 50 5MUSES objects either do not have redshift

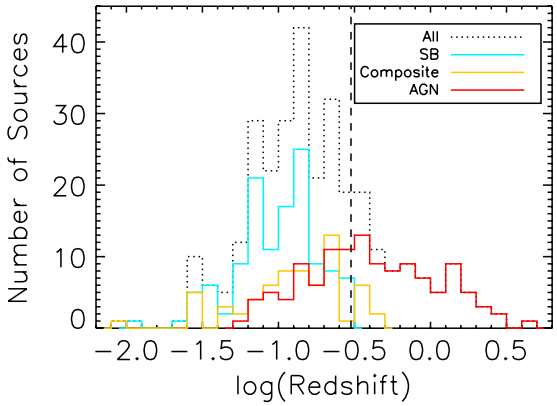

Figure 1. Redshift distribution for 309 out of 330 sources in the 5MUSES sample (dotted line). The blue, yellow, and red lines represent the distribution for SB, composite, and AGN-dominated sources, respectively. The dashed vertical line indicates the redshift cut of $z < 0.3$ on which this paper is focused.

(A color version of this figure is available in the online journal.)

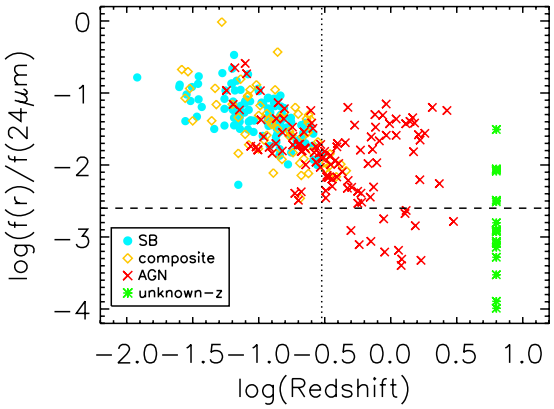

Figure 2. Ratio of flux densities at the SDSS r band to the MIPS 24 μm band vs. redshift for 5MUSES sources. The blue circles, yellow diamonds, and red crosses represent the SB, composite, and AGN sources, respectively. The green stars represent sources without redshifts. The dotted vertical line indicates our redshift cut of $z < 0.3$. The dashed line indicates $\log[f_\nu(r)/f_\nu(24\,\mu\mathrm{m})] = -2.6$. All 13 objects with $\log[f_\nu(r)/f_\nu(24\,\mu\mathrm{m})] < -2.6$ are located at $z > 0.3$. Seventeen out of 21 unknown-z sources have $\log[f_\nu(r)/f_\nu(24\,\mu\mathrm{m})] < -2.6$, and are thus most likely to lie at $z > 0.3$.

(A color version of this figure is available in the online journal.)

information from the literature, or their IRS spectra are characterized by featureless power-law continua, which cannot yield redshifts. We obtained redshifts for some of these sources by using the double spectrograph instrument on the Palomar 200 inch Telescope in 2009B and 2010A terms. The optical data are reduced with the IRAF software using the standard routines for bias subtraction, flat-fielding, sky background removal, and wavelength calibration. Finally, for sources with multiple emission line features, redshifts are derived using all available emission lines.

2.3. The Redshift Completeness

Combining the IRS, Palomar spectra, and literature work, we found secure redshift measurements for 309 objects out of the 330 sources in 5MUSES (94%). The redshift distribution of 5MUSES is shown in Figure 1. We also show the redshift distribution for starburst (SB), composite, and AGN-dominated sources, respectively, which have been classified based on their apparent 6.2 μm PAH EWs[7] (Wu et al. 2010). Since we are only interested in the redshift range of $z < 0.3$ for this study, the relevant redshift completeness is close to 1 for two reasons: (1) the sources for which we are not able to find redshifts from 80 minutes of integration time on the Palomar 200 inch telescope have very low r band to 24 μm band flux ratios $f_\nu(r)/f_\nu(24\,\mu\mathrm{m})$. As can be seen from Figure 2, objects with low $f_\nu(r)/f_\nu(24\,\mu\mathrm{m})$ ratios (i.e., $\log[f_\nu(r)/f_\nu(24\,\mu\mathrm{m})] < -2.6$) are more likely to have high redshifts ($z > 0.3$; see also Dey et al. 2008). (2) The IRS spectra of the sources without redshifts are characterized by a featureless power-law continuum in the mid-IR. This indicates that they are most likely AGN-dominated. It can be seen from Figure 1 that the median redshift for AGN-dominated sources is much higher than SB or composite sources. The median redshift for sources with 6.2 μm PAH EW$> 0.2\,\mu$m is 0.13, while it is 0.40 for sources with 6.2 μm PAH EW $< 0.2\,\mu$m. Thus, these power-law sources are much more likely to lie at the high end of the redshift distribution.

For this study, we focus on objects with $z < 0.3$, which includes 226 objects. Among the 21 (330–309) sources without redshift, only 4 do not have very low $f_\nu(r)/f_\nu(24\,\mu\mathrm{m})$ ratios, e.g., their $\log[f_\nu(r)/f_\nu(24\,\mu\mathrm{m})] > -2.6$, and might be located at $z < 0.3$. This indicates that the redshift completeness for our sample at $z < 0.3$ is $\gtrsim$98%.

3. METHODOLOGY

3.1. The Incompleteness Correction

The targets for 5MUSES are randomly selected based on $f_\nu(24\,\mu\mathrm{m}) > 5$ mJy after excluding the resolved objects. Understanding the selection function for 5MUSES is crucial for building the LF. Because we exclude extended objects, it is likely that we have excluded more nearby objects than those at higher redshifts. Thus, when we derive the number density, instead of applying a uniform correction factor of ∼3.4 (1111/330), we need to investigate the selection effect in individual redshift bins before we build our LF.

Redshift information is not available for all the sources in the parent sample of 5MUSES, thus we use the redshift catalog of Papovich et al. (2006) for the XFLS field to understand the redshift distribution when a flux limit of 5 mJy is imposed. Papovich et al. (2006) observed the XFLS field using the Hectospec instrument on MMT for five positions covering a 1 deg diameter field of view individually. Then they combined redshifts from Hectospec with redshifts from the Sloan Digital Sky Survey (SDSS), and reached a completeness of ∼90% at $f_\nu(24\,\mu\mathrm{m}) > 1$ mJy in the 3.3 deg^2 of their survey field. These authors also provided the completeness factors at different flux limits, which we use to derive the final number counts at $f_\nu(24\,\mu\mathrm{m}) > 5$ mJy in the XFLS field. Then we divide the number of objects in different redshift bins by the total number of objects in the XFLS field, and derive the fractional contribution of number counts in this field at $f_\nu(24\,\mu\mathrm{m}) > 5$ mJy. Using this as a reference, we predict the number of objects in the corresponding redshift bins for the 5MUSES sample. Then we divide the predicted number counts by the number of objects we have observed and obtain the correction factor in each redshift bin. Finally, we fit a second-order polynomial to the data and this gives us the completeness correction factor $\omega_i(z)$, which is then used to correct for the incompleteness at different redshifts.

[7] Sources with 6.2 μm PAH EW $> 0.5\,\mu$m are SB-dominated; sources with $0.2\,\mu\mathrm{m} <$ PAH EW $< 0.5\,\mu$m are composite; and sources with PAH EW $< 0.2\,\mu$m are AGN-dominated.

3.2. The $1/V_{max}$ Method

We limit our study of the mid-IR LF to $z < 0.3$ because the rest-frame 24 μm band[8] moves outside the IRS spectrum beyond $z = 0.3$. In addition to that, our relatively bright flux limit of $f_\nu(24\,\mu\mathrm{m}) > 5$ mJy results in a fast decrease of the number of objects as redshift increases, which would yield results that have low statistical significance at high redshift.

In this study, we use the $1/V_{\max}$ method (Schmidt 1968) to derive the LF, which does not require any assumption about the shape of the LF. The $1/V_{\max}$ method counts galaxies within a volume. $V_{\max}$ is calculated individually for each source in our sample as the maximal volume within which that galaxy is detectable in this survey. The availability of 5–35 μm IRS spectrum allows us to accurately make k-corrections based on the observed SED shape for individual galaxies. We first derive the k-correction for each object, and then move the galaxy to the redshift where its 24 μm observed flux reaches the limit of this sample, 5 mJy. The maximum comoving volume is calculated as

$$V_{i,\max} = \int_{z_{\rm low}}^{z_{\rm high}} \frac{dV}{dz} dz, \quad (1)$$

where $[z_{\rm low}, z_{\rm high}]$ is the redshift range of interest. For our study, we ignore sources with $z < 0.02$, while $z_{\rm high}$ is the lower of the two: (1) the maximum redshift considered in this study, 0.3, or (2) the maximum redshift a source can be detected at the limiting observed 24 μm flux of 5 mJy. The uniformity of the distribution of galaxies is tested by checking the $V/V_{\max}$ values and we find $\langle V/V_{\max}\rangle = 0.54$ for the sources used in this study.

The LF is then derived by using the following formula (Schmidt 1968):

$$\phi = \frac{4\pi}{\Omega} \Sigma \frac{1}{V_{i,\max}} \frac{1}{\Delta \log \mathrm{L}} \omega_i, \quad (2)$$

where Ω is the total survey area of the 5MUSES sample (40.6 deg^2), $V_{i,\max}$ is the comoving volume over which the ith galaxy could be observed, $\Delta\log L$ is the size of the luminosity bin, and ω_i is the completeness correction factor for the ith galaxy. ω_i is a function of redshift and was calculated in Section 3.1. We divide the sources into seven luminosity bins, and calculate the value of ϕ in each bin. The uncertainties include both the Poisson noise statistics on the number of sources used in the measurement and the uncertainty associated with the completeness correction factor ω_i. As can be seen from Figure 3, the uncertainty of ω_i is rather large, mainly due to the small number of objects in each redshift bin in XFLS at $f_\nu(24\,\mu\mathrm{m}) > 5$ mJy, so we assign an uncertainty of 40% to ω_i, which is the average uncertainty for the data points we use to calculate the correction factor. Because our k-corrections are made directly from the source SED, we have almost negligible uncertainties associated with the conversion from the observed flux to the rest-frame luminosities. For the LFs presented in this paper, we do not include noise from the cosmic variance since we sample several widely distributed directions.

3.3. Spectral Decomposition in the Mid-IR

The mid-IR SED of star-forming galaxies and AGN show distinctly different spectral features. As a result, the availability of 5–35 μm IRS spectra for the 5MUSES sample allows us to disentangle the SF and AGN contribution to the galaxy luminosity. Star-forming galaxies often display broad emission features, which are generally attributed to the emission from PAHs. AGNs, on the other hand, are usually characterized by a featureless power-law continuum (except for a few high-ionization fine-structure lines) and their mid-to-far-IR continuum slopes are normally flatter than star-forming galaxies. A combination of one SB template and a power-law continuum with a free spectral index have often been used to decompose galaxy spectra into SF and AGN components for high-redshift galaxies (Sajina et al. 2008; Pope et al. 2008; Menéndez-Delmestre et al. 2009; Murphy et al. 2009). The high signal-to-noise ratio IRS data of the 5MUSES sample allow us to take into account detailed mid-IR features and decompose the galaxy spectra much more accurately. Among mid-IR spectral features (PAH strength, continuum slopes, silicate strength, fine-structure lines, etc.), PAH strength or the IR continuum slopes are arguably the most commonly used indicators for SF, so we select our templates mainly based on these two parameters. We start from our empirical SED template library (Wu et al. 2010), which has included star-forming galaxies, ULIRGs, and PG/2MASS quasars, and select 15 star-forming galaxy (6.2 μm PAH EW $> 0.5\,\mu$m) templates and 10 quasar templates, covering as large a range of PAH strengths and slope variations as possible. Then we perform a least-χ^2 fit for each combination of an SF template and a quasar template to find the most likely coefficients that would describe the observed 5MUSES spectrum as a linear combination of the two templates. In the upper panels of Figure 4, we show examples of decomposition of IRS spectra of typical SB-dominated, composite, and AGN-dominated sources.

Statistical constraints on the SF contribution. Rather than directly adopting the SF fraction at 15 μm from the best fit, we build the probability density function (pdf) of the SF fraction by weighting the values of SF fraction for each trial fit by $\exp(-\chi^2/2)$. Then the SF fraction is taken to be the median of the resulting pdf and the 1σ uncertainty is taken to be the 16th–84th percentile range. In the lower panels of Figure 4, we show the corresponding pdf for each source and the SF fraction and its associated uncertainties are also indicated on the plot.

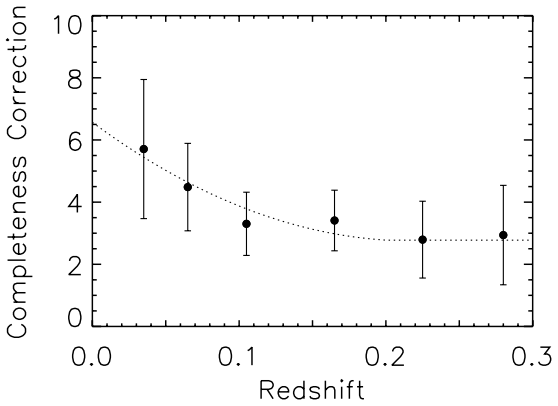

Figure 3. Completeness correction factor for 5MUSES vs. redshift. Instead of using an average correction factor of ∼3.4 (1111/330), we benchmark our sample with the XFLS, where redshifts are available for this field. We first derive the fractional contribution of number counts in different redshift bins for the XLFS field at $f_\nu > 5$ mJy. Using this as a reference, we predict the number counts in each redshift bin for the 5MUSES sample. Then we divide the predicted number of objects by the observed number and obtain the completeness correction in each redshift bin. Finally, we use a second-order polynomial to fit the data and obtain the completeness correction factor as a function of redshift. The error bars represent the Poisson noise.

[8] Here we refer to the MIPS 24 μm filter, instead of the monochromatic 24 μm continuum.

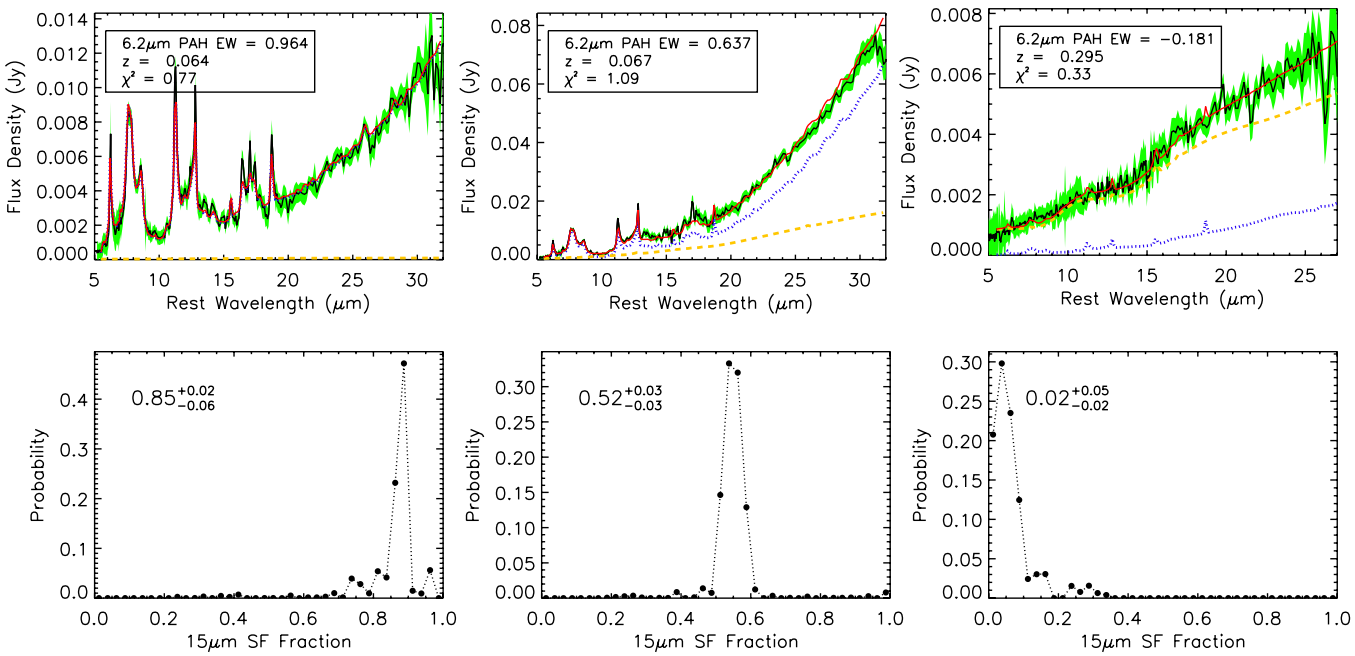

Figure 4. (a) Upper panels: examples of our decomposition on the IRS spectra for typical starburst, composite, and AGN-dominated sources in 5MUSES. The black solid line is the IRS spectrum and the green shaded region indicates the uncertainties. The blue dotted line is the scaled star formation galaxy template, the yellow dashed line is the scaled quasar template, and the red solid line is the best-fit composite spectrum. The 6.2 μm PAH EWs (a negative value indicates an upper limit), redshifts of the objects, as well as the reduced χ^2 values, are also shown in the plot. (b) Lower panels: the probability density function for the star formation fraction at 15 μm for each corresponding object. The median fraction and its 16th to 84th percentile range is also indicated.

(A color version of this figure is available in the online journal.)

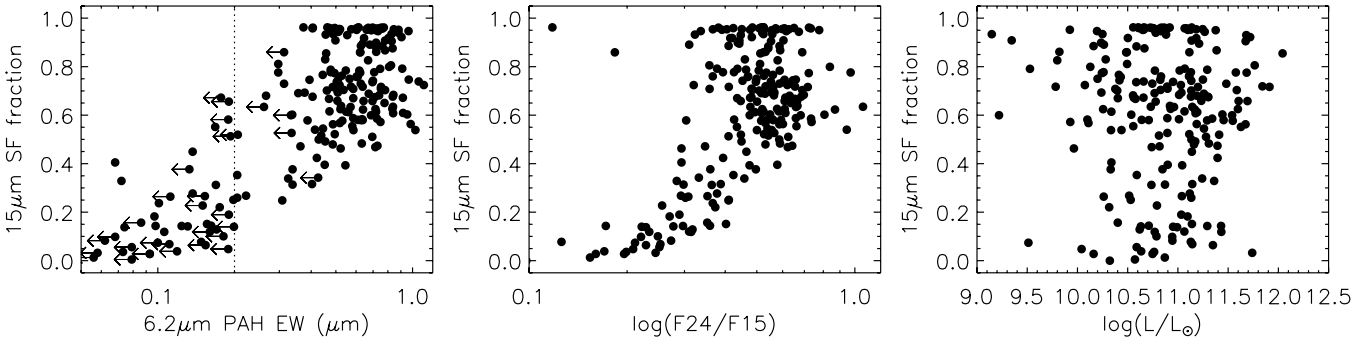

Figure 5. Left panel: the SF fraction at 15 μm vs. the 6.2 μm PAH EW. The dotted line indicates 6.2 μm PAH EW = 0.2 μm. Middle panel: the SF fraction vs. the mid-IR continuum slope of $f_\nu(24\mu\text{m})/f_\nu(15\,\mu\text{m})$. Both the PAH EW and continuum slope are correlated with the SF fraction at 15 μm with scatter. The two sources in the middle panel with very low $f_\nu(24\,\mu\text{m})/f_\nu(15\,\mu\text{m})$ ratios and high SF fractions have their mid-IR spectra dominated by PAH emission, while their continuum slopes do not rise quickly. This also indicates that the continuum slope alone has a high uncertainty when it is used as an SF indicator. Right panel: the SF fraction vs. the infrared luminosity. There is no clear correlation between these two parameters. Note that at the high-luminosity end, we do not observe many objects with a low SF fraction. This is because we have not included very high luminosity sources in this study ($z < 0.3$).

As discussed earlier, the 6.2 μm PAH EW and the continuum slope have often been used as indicators of SF activities. We compare the 6.2 μm PAH EW and continuum slope of $f_\nu(24\,\mu\text{m})/f_\nu(15\,\mu\text{m})$ versus SF fraction estimated from the probability distribution in the left and middle panels of Figure 5. Our median likelihood SF fraction clearly correlates with both parameters while the scatter is quite significant for intermediate values of $f_\nu(24\,\mu\text{m})/f_\nu(15\,\mu\text{m})$ ratios. Note however that for $f_\nu(24\,\mu\text{m})/f_\nu(15\,\mu\text{m}) < 0.3$, all but two sources have very low SF fraction, suggesting that very flat mid-IR slopes are a strong discriminator for AGNs. We also note that some sources, even though they have very large PAH EWs (>0.5 μm), have SF fractions only $\gtrsim$0.5. This could be due to the fact that we are looking at the SF fraction at 15 μm in this study, while the contribution to the total IR luminosity is very likely to be dominated by SF. On the other hand, we also need to point out that the SF fraction we derive has at least ~20% uncertainty. Finally, we plot the SF fraction versus the IR luminosity for each source in the right panel of Figure 5 and we do not observe any correlation. This indicates that luminosity itself provides limited information on the energy source of a galaxy. Clearly, there is no single parameter that could be used to determine the SF fraction accurately, thus a combination of a few is indeed needed in order to constrain the relative contributions of SF and AGN.

4. RESULTS

4.1. The 24 μm and 15 μm Luminosity Functions at $z < 0.3$

From the 5–35 μm IRS spectrum of the 5MUSES sample, we can directly estimate the rest-frame MIPS-equivalent 24 μm luminosities. Using the $1/V_{\rm max}$ method, we have derived the 24 μm LF for sources with $z < 0.3$. Our 24 μm LF is shown

Table 1
Mid-IR Luminosity Function Derived from the $1/V_{\rm max}$ Method

$\log L_{24\,\mu{\rm m}}$ ($L_\odot$)	ϕ (Mpc^{-3} dex$^{-1}(L)$)	$\log L_{15\,\mu{\rm m}}$ ($L_\odot$)	ϕ (Mpc^{-3} dex$^{-1}(L)$)	$\log L_{24\,\mu{\rm mSF}}$ ($L_\odot$)	ϕ (Mpc^{-3} dex$^{-1}(L)$)	$\log L_{15\,\mu{\rm mSF}}$ ($L_\odot$)	ϕ (Mpc^{-3} dex$^{-1}(L)$)
8.95	$4.66 \pm 2.47 \times 10^{-3}$	8.75	$3.18 \pm 1.75 \times 10^{-3}$	8.95	$3.41 \pm 1.80 \times 10^{-3}$	8.25	$3.36 \pm 2.01 \times 10^{-3}$
9.40	$2.62 \pm 1.16 \times 10^{-3}$	9.15	$2.58 \pm 1.12 \times 10^{-3}$	9.40	$2.36 \pm 1.05 \times 10^{-3}$	8.75	$2.41 \pm 1.18 \times 10^{-3}$
9.70	$1.46 \pm 0.67 \times 10^{-3}$	9.45	$1.58 \pm 0.69 \times 10^{-3}$	9.70	$1.13 \pm 0.53 \times 10^{-3}$	9.15	$2.40 \pm 1.11 \times 10^{-3}$
10.00	$6.49 \pm 2.76 \times 10^{-4}$	9.75	$5.96 \pm 2.57 \times 10^{-4}$	10.00	$5.73 \pm 2.45 \times 10^{-4}$	9.45	$9.01 \pm 4.01 \times 10^{-4}$
10.35	$3.37 \pm 1.70 \times 10^{-4}$	10.05	$2.89 \pm 1.54 \times 10^{-4}$	10.35	$3.06 \pm 1.59 \times 10^{-4}$	9.75	$4.87 \pm 2.25 \times 10^{-4}$
10.60	$9.16 \pm 4.09 \times 10^{-5}$	10.35	$6.95 \pm 3.07 \times 10^{-5}$	10.60	$4.58 \pm 2.17 \times 10^{-5}$	10.05	$8.54 \pm 3.88 \times 10^{-5}$
10.85	$3.40 \pm 1.51 \times 10^{-5}$	10.75	$1.36 \pm 0.60 \times 10^{-5}$	10.85	$1.64 \pm 0.81 \times 10^{-5}$	10.35	$1.87 \pm 0.92 \times 10^{-5}$

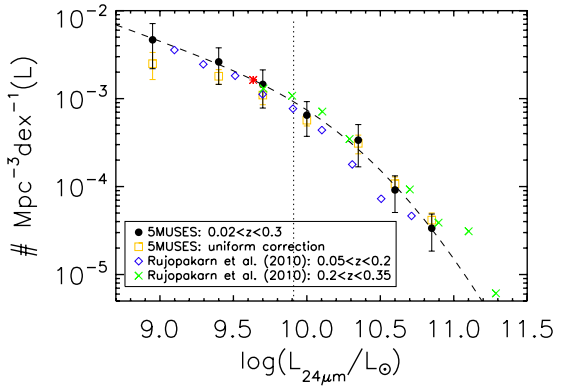

Figure 6. Rest-frame MIPS 24 μm luminosity function at $z < 0.3$ derived from the 5MUSES sample using the $1/V_{\rm max}$ method (black circles). The yellow squares represent the LF if we were to apply a uniform completeness correction factor of ∼3.4. The blue diamonds and green crosses represent the 24 μm LFs at $0.05 < z < 0.2$ and $0.2 < z < 0.35$ derived by Rujopakarn et al. (2010). The dashed line is the fit to the data points of our 24 μm LF assuming a double power-law exponential function. The knee ($L^\star$) of the LF is represented by the red star in the plot. The dotted line denotes the luminosity calculated at the median redshift of this sample corresponding to the flux limit at 24 μm.

(A color version of this figure is available in the online journal.)

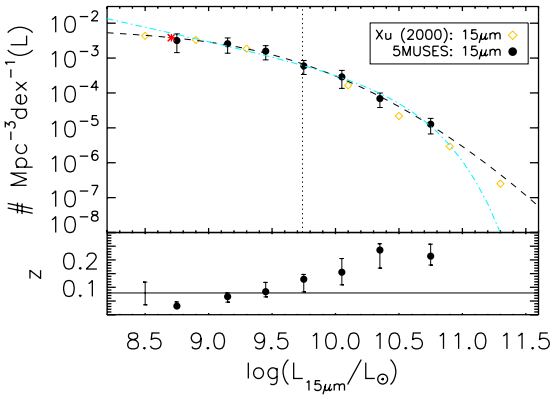

Figure 7. Top panel: the monochromatic 15 μm luminosity function at $z < 0.3$ derived from the 5MUSES sample (filled circles). The dashed line is the fit to the data points assuming a double power-law exponential function. The blue dot-dashed line represents the fit with a Schechter function to our data. The knee ($L^\star$) of the LF is represented by the red star. The dotted line corresponds to the luminosity calculated at the median redshift of our sample for a galaxy at the flux limit. The local 15 μm luminosity function from Xu (2000) is overplotted with the yellow diamond for comparison. Our 15 μm LF is in excellent agreement at the faint end with the *ISO* 15 μm LF by Xu (2000), but is slightly higher at the bright end. Bottom panel: the median redshift in each luminosity bin we have used to derive our LF. The solid line represents the median redshift of Xu's sample.

(A color version of this figure is available in the online journal.)

in Figure 6 and the corresponding data points are reported in Table 1. We adopt a double power-law exponential function (Saunders et al. 1990) to fit our LF:

$$\phi(L) = \frac{dN(L)}{dV d\log_{10}(L)} = \phi^\star \left(\frac{L}{L^\star}\right)^{1-\alpha} \exp\left\{-\frac{1}{2\sigma^2}\log_{10}^2\left[1+\left(\frac{L}{L^\star}\right)\right]\right\}. \quad (3)$$

The dashed line is the fit to our data by running mpfit.pro. The uncertainties on the fitting parameters are derived with 1000 Monte Carlo realizations and they are reported in Table 2. The dotted line denotes the luminosity calculated at the median redshift of our sample corresponding to the 24 μm flux limit. Note that 5 mJy is the flux limit on the observed 24 μm, while the flux limit we use here is taken to be the rest-frame 24 μm flux density corresponding to the galaxy with $f_{\rm obs}(24\,\mu{\rm m}) = 5$ mJy and maximum k-corrected. In Figure 6, we have also included the 24 μm LFs by Rujopakarn et al. (2010) for comparison. Our LF is in good agreement with Rujopakarn et al. (2010) at the low end, while at the high end our data points are located between the $0.05 < z < 0.2$ and the $0.2 < z < 0.35$ LFs they have derived. This indicates that in the redshift range we derive our LF, evolution is probably already at work, as will be addressed in more detail later on.

We then compute the rest-frame 15 μm monochromatic[9] LF for our sample. The LF at this wavelength has been extensively studied in the local universe (Xu 2000; Pozzi et al. 2004; Matute et al. 2006) as well as at high redshift (Le Floc'h et al. 2005; Magnelli et al. 2009) to explore the evolution of galaxy populations. We repeat the steps used for calculating the 24 μm LF and derive the 15 μm LF for the 5MUSES sample. In the upper panel of Figure 7, we plot our 15 μm LF with solid circles and the corresponding data points are reported in Table 1. The dotted line denotes the luminosity calculated at the median redshift of this sample corresponding to the 15 μm flux limit. As expected, the completeness level at 15 μm is much lower than at 24 μm, since this is a 24 μm selected sample at $z < 0.3$. The dashed line is the fit to our LF with a double power-law exponential function. During our fit, we fixed the faint-end slope to $\alpha = 1.2$, which has been well determined from similar studies in the local universe. The results of the fitting parameters are reported in Table 2. For comparison, we also overplot the local 15 μm LF from Xu (2000) derived using ISOCAM observations. Similar to what we have observed when we compare our 24 μm LF with Rujopakarn et al. (2010), the 5MUSES LF is in good agreement with Xu's LF at the low end,

[9] The monochromatic luminosity is calculated within a width of 1 μm.

Table 2
Results of the Fits to the Mid-IR Luminosity Functions

LF (Wavelength)	α	σ	$\log L^{\star}(L_{\odot})$	$\log \phi(\mathrm{Mpc}^{-3}\ \mathrm{dex}^{-1}(L))$	$\rho(L_{\odot}\ \mathrm{Mpc}^{-3})$
LF (24 μm)	1.61 ± 0.62	0.57 ± 0.30	9.63 ± 1.42	−2.72 ± 0.98	$3.36 \pm 1.06 \times 10^{7}$
LF (15 μm)	1.20 (fixed)	0.65 ± 0.22	8.71 ± 1.35	−2.24 ± 0.99	$1.54 \pm 0.32 \times 10^{7}$
LF (24 μm SF)	1.63 ± 0.28	...	10.37 ± 0.28	−3.27 ± 0.40	$2.61 \pm 1.14 \times 10^{7}$
LF (15 μm SF)	1.38 ± 0.20	...	9.76 ± 0.16	−2.93 ± 0.26	$8.99 \pm 2.20 \times 10^{6}$

while our LF is slightly higher at the high-luminosity end. This can be explained by the differential evolution effect. The density or luminosity evolution with redshift have been extensively studied (Le Floc'h et al. 2005; Pérez-González et al. 2005; Magnelli et al. 2009). Evolution affects different luminosity bins by different amounts because they are populated from different redshift ranges. In the lower panel of Figure 7, we plot the median redshift in each luminosity bin as a solid circle and the 16th and 84th percentile as the error bar. The median redshift ($z = 0.09$) for Xu's sample has also been plotted (solid line) together with its 1σ population dispersion. Although the median redshift for the sources used in this study is 0.12, it is clear that the high-luminosity end is dominated by sources at higher redshift, thus our slightly higher LF at the bright end is almost certainly a result of that difference.

In addition to using the double power law to fit the LF, we have also attempted using a single Schechter function. In Figure 7, we overplot the fit with the Schechter function as the blue dot-dashed line. Although the Schechter function can fit our data reasonably well, the fit is rather poor in both the faint and bright ends when the data points from the *ISO* 15 μm LF by Xu (2000) are included.

4.2. The Star Formation Luminosity Function

In the previous subsection, we have shown that the 15 μm LF need to be fit with a double power-law exponential function because the bright-end slope of the LF is clearly flatter than the Schechter function. This is in contrast to UV LFs, which display much steeper slopes at the high-luminosity end. As both the UV and IR luminosities trace active SF, with the IR being the reprocessed portion of the UV, one would expect similar behaviors of the LFs of the UV and IR emission. Using *Spitzer* IRAC observations of the Bootes field, Huang et al. (2007) have shown that the 8 μm LF of a sample of star-forming galaxies does indeed follow the shape of a Schechter function. More recently, using AKARI data, Goto et al. (2011) have shown that after removing the optically identified AGN, their IR LF becomes much steeper. Using *Spitzer* IRS spectra, Fu et al. (2010) have studied the 15 μm LF at $z = 0.7$ and constrained the slope of the SF LF at the high-luminosity end using a Schechter function. So the flatter LFs we are deriving probably reflect AGN contributions to the IR, and we will verify this hypothesis in what follows. In Section 3.3, we have shown our method of decomposing the SF/AGN contribution from the mid-IR spectra of 5MUSES sources and estimated the SF fraction by taking the median likelihood of the pdf. Now we derive the SF LFs at 15 and 24 μm for 5MUSES at $z < 0.3$.

Local 15 μm SF LF. Using the median estimate of the SF fraction for each object, we derive the 15 μm SF luminosity by multiplying the 15 μm monochromatic continuum luminosity by the SF fraction at the corresponding wavelength obtained from spectral decomposition. The resulting individual SF luminosities are then used to build the SF LF. In the left panel of Figure 8, we show the 15 μm SF LF (red squares) at $z < 0.3$. The black dotted line is a fit to the LF adopting the Schechter function (Schechter 1976):

$$\phi(L) = \frac{dN(L)}{dV d\log_{10}(L)} = \phi^{\star}\left(\frac{L}{L^{\star}}\right)^{1-\alpha} \exp\left(-\frac{L}{L^{\star}}\right). \quad (4)$$

We overplot the local 15 μm LF for normal spiral and SB galaxies by Pozzi et al. (2004) as the blue crosses. These authors analyzed data from the ELAIS southern fields and excluded AGNs in their study. Their SF LFs appear to be in good agreement with our results. We also overplot the total 15 μm LF as the black filled circles in the left panel of Figure 8, and the dashed line is a fit to the total 15 μm LF with a double power-law exponential function. The two LFs, the total and the SF LFs at 15 μm, differ significantly at $L_{15\,\mu\mathrm{m}} > 10^{10}\ L_{\odot}$. This is presumably due to the AGN contribution at high luminosities. The AGN LFs display distinctly different shapes from SF LF as has been shown by Matute et al. (2006), Hopkins et al. (2007), etc. When the luminosity increases, the AGN contribution also increases progressively. This AGN component reveals its presence in the total 15 μm LF by requiring a different slope in the fit at high luminosity. In Figure 8, we have overplotted the 15 μm AGN LF as green diamonds and fit the data with a double power-law exponential function. Clearly, the AGN LF presents a much shallower slope at high luminosities. On the other hand, the 15 μm SF LF drops quickly at the bright end and could be fit well with a Schechter function. This has already been seen in the local universe for the 8 μm LF of star-forming galaxies by Huang et al. (2007), as well as the 15 μm AGN-corrected LF at $0.6 < z < 0.8$ by Fu et al. (2010).

Local 24 μm SF LF. We repeat the same steps used to derive the 15 μm SF LF at 24 μm and show the 24 μm SF LF in the right panel of Figure 8. Again, we observe the departure of the total and SF LFs at 24 μm at the bright end and the best-fit parameters are reported in Table 2. Rujopakarn et al. (2010) have identified AGNs from optical spectroscopy and derived 24 μm SF LF in several redshift bins. Their comparison of the 24 μm total LF and the 24 μm SF LF shows a very similar trend as what we have observed from our sample. We also overplot their 24 μm SF LFs at $0.05 < z < 0.2$ and $0.2 < z < 0.35$ as the blue diamonds and green crosses in Figure 8.

4.3. Discussion

As the main luminous phenomena in the universe, SF and AGN activities have been extensively studied across all wavelengths. Despite the amount of effort to quantify the SF/AGN contribution and explore its evolution with luminosity/redshift, no fair comparison can be made unless truly equivalent samples are studied. Our 5MUSES sample, after correcting for selection effects, essentially defines a relatively bright IR selected unbiased sample, which is critical for understanding the galaxy evolution and energy balance in a cosmological context. In this subsection, we discuss how the SF/AGN fraction varies with wavelength, luminosity, and redshift.

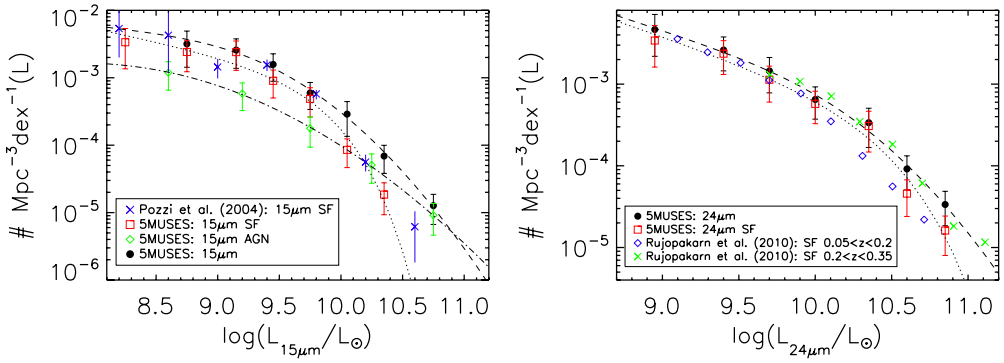

Figure 8. (a) Left panel: a comparison of the 15 μm luminosity function (black filled circles) and the 15 μm star-formation luminosity function (red squares). The dashed line and the dotted line are the fits to the two LFs. The blue crosses represent the local AGN-excluded LF by Pozzi et al. (2004) and appear to be in good agreement with our 15 μm SF LF. The green diamonds represent the AGN LF derived from our sample and the dot-dashed line provides a fit to the AGN LF with a double power-law exponential function. (b) Right panel: a comparison of the MIPS 24 μm luminosity function (black filled circles) and star-formation luminosity function (red squares). The dashed lines are the fits to the total LFs with a double power-law exponential function, while the dotted lines are the fits to the SF LFs with a Schechter function. The blue diamonds and green crosses, respectively, represent the 24 μm SF LFs at $0.05 < z < 0.2$ and $0.2 < z < 0.35$ by Rujopakarn et al. (2010).

(A color version of this figure is available in the online journal.)

4.3.1. SF/AGN Fraction at Mid- and Total IR

In Sections 4.1 and 4.2, we have derived the 15 μm LF for the entire sample at $z < 0.3$, as well as the 15 μm SF LF. Integrating the differential LF, we estimate the luminosity density at 15 μm to be $(1.5 \pm 0.3) \times 10^7\ L_\odot$ Mpc^{-3} to which the SF contribution is $(9.0 \pm 2.2) \times 10^6\ L_\odot$ Mpc^{-3}. This gives an SF fraction of $\sim$58% $\pm$ 19% to the integrated 15 μm luminosity density. Then we extrapolate our results at 15 μm to the total IR. Following the technique described in Wu et al. (2010), we convert 15 μm luminosity density to the total IR luminosity density for the AGN component and the SF component separately. Although the uncertainty in the SF fraction in total IR will be significantly higher because the error in converting $L_{15\,\mu m}$ to L_{IR} also comes into play, this is still a critical quantity to obtain, especially for studies of the distant universe, where the PAH features are more difficult to measure, or the PAHs in high-redshift galaxies might have different properties (e.g., larger EWs) for similar dust mass fractions. We find that the SF contribution comes up to 83% of the total IR luminosity density. This is understandable as the SED of star-forming galaxies is much steeper than that of the AGN, thus the FIR emission will be dominated by SF. If we convert the IR luminosity for the SF component to the SF rate and integrate over cosmic time, we find that our derived SF rate density is consistent with the dust extinction corrected values of Hopkins & Beacom (2006; see also Madau et al. 1996; Lilly et al. 1996). We repeat the same exercise at 24 μm. Integrating the 24 μm LF, we find the luminosity density at 24 μm to be $(3.4 \pm 1.1) \times 10^7\ L_\odot$ Mpc^{-3}, while the SF luminosity density is $(2.6 \pm 1.1) \times 10^7\ L_\odot$ Mpc^{-3}. This gives an SF fraction of $\sim$78% $\pm$ 42% at 24 μm, higher than the number at 15 μm, while consistent with the concept that SF becomes more dominant at longer wavelength. We again convert the integrated 24 μm luminosity to total IR luminosity density for star-forming systems and AGN separately and find the SF fraction to increase to $\sim$89%, in agreement with the estimate from 15 μm. If we take the average of the two (86%), then the SF fraction in the total IR luminosity density we have derived is higher than the study of Veilleux et al. (2009) for local ULIRGs, while more consistent with Nardini et al. (2008). However, we need to bear in mind that both Veilleux and Nardini study the ULIRG population, while the luminosity of our sample is mostly in the range of $10^{9.0}\ L_\odot$ to $10^{12.0}\ L_\odot$. The recent study of Petric et al. (2011) derived an average AGN fraction of 12% in the total IR for LIRGs, consistent with our estimate.

As already noted (Figure 8), the 15 μm SF LF departs from the 15 μm LF most significantly at the bright end, and this is again observed at 24 μm. It suggests that the SF fraction is a function of luminosity (Yuan et al. 2010; Hopkins et al. 2010). In order to quantify how this fraction varies, we plot in the left panel of Figure 9 the SF fraction at 15 μm versus the 15 μm luminosity. We divide our sources into several luminosity bins and estimate the contribution of SF in each luminosity bin. The error bar represents the Poisson noise in each bin. We find that the SF fraction decreases as the 15 μm luminosity increases. This is expected since AGNs play a more important role in the energy budget for more distant, thus more luminous, sources in our sample (see Figure 10). In the right panel of Figure 9, we plot the SF fraction at 24 μm versus the 24 μm luminosity. We again observe a trend of the SF fraction decreasing with larger $L_{24\,\mu m}$, however, the decline is much milder and the SF fraction is also higher at 24 μm as compared to the 15 μm. Finally, we convert the 24 μm SF luminosity and 24 μm luminosity to L_{SFIR} and L_{IR}, and show in the left panel of Figure 10 how the total IR SF fraction varies as a function of IR luminosity, while in the right panel we display the SF fraction versus redshift. We find that the SF fraction decreases with redshift, while there is little dependence of SF fraction with L_{IR}. The decrease of SF fraction with redshift can be understood since our sample selects a higher fraction of AGN-dominated sources as the redshift increases (see also Figure 1). We observe a mildly decreasing, or rather flat correlation between the IR SF fraction and L_{IR} because (1) at $z < 0.3$, the luminosity of our sources only ranges from $10^9\ L_\odot$ to $10^{12}\ L_\odot$ and the majority of the sources included in this study are SF dominated and (2) even for a source dominated by a powerful AGN in the mid-IR, its FIR emission could still be powered by SF, thus SF dominates the total IR luminosity. Because of the dominant contribution of SF in the FIR luminosity, we do not observe a strong dependence on L_{IR} for the SF fraction. This suggests that the mid-IR might be a more reliable wavelength if one wants to study the SF/AGN fraction. The launch of the *Herschel Space Telescope* has opened a new window for observing the cold dust in the universe. Data from large area

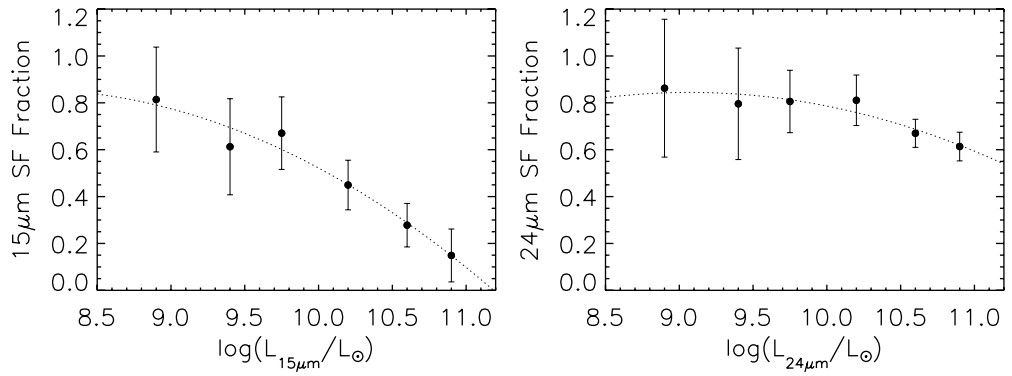

Figure 9. (a) Left panel: the fractional contribution of the SF luminosity in each luminosity bin at 15 μm. The dotted line is a second-order polynomial fit to the data. (b) Same as (a), but for 24 μm.

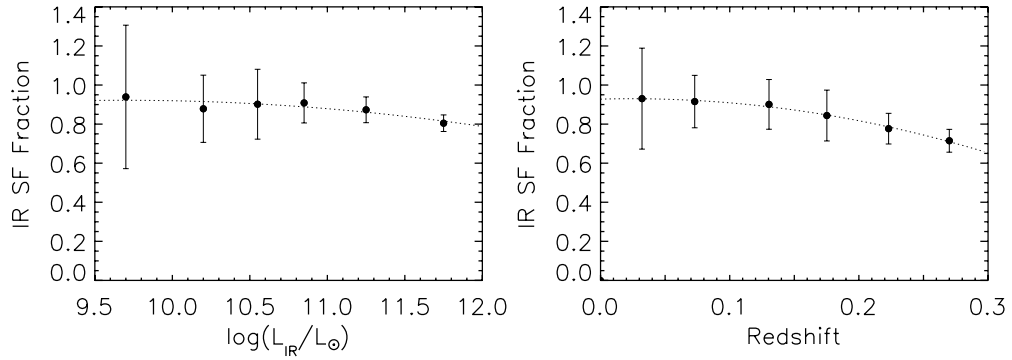

Figure 10. (a) Left panel: the fractional contribution of the star-formation luminosity in each luminosity bin in the total IR luminosity, converted from the results at 24 μm. The dotted line is a second-order polynomial fit to the data. (b) The SF fraction in the total IR luminosity vs. the redshift. The dotted line is a second-order polynomial fit to the data.

Herschel surveys, such as *HerMES* (Oliver et al. 2010), will provide essential constraints on the FIR emission for sources in our sample, allowing a direct decomposition of SF/AGN in the total IR luminosity. Future studies using 70–500 μm data from *Herschel* will help to further constrain the SF fraction in the total IR luminosity density, and the associated uncertainties.

4.3.2. Comparison with LF at $z = 0.7$

In this section, we compare the LFs derived from the 5MUSES sample with relevant work at higher redshift to understand the evolution effects. The median redshift for our LF is 0.12. When compared with the 15 μm LF by Xu (2000) from *ISO* work, we find in general good agreement between our LF and Xu's LF, while at the high-luminosity end the two LFs show some discrepancy. Because of the higher median redshift of the objects in the high-luminosity bin of our LF, this small discrepancy with the local LF hinted at evolution effects as a function of redshift. We then compare our work with studies at high redshift. 15 or 24 μm LFs and LFs for star-forming galaxies have been derived by several different groups (Le Floc'h et al. 2005; Magnelli et al. 2009; Rujopakarn et al. 2010; Fu et al. 2010). In addition to deriving the rest-frame 15 μm LF from the 5MUSES sample, the availability of 5–35 μm IRS spectra also allowed us to decompose the SF and AGN contributions to the IR SED in a more precise way, and thus derive the SF LF using the SF luminosity in each object from our sample. The most relevant work at higher redshift is at $z = 0.7$ by Fu et al. (2010). These authors use the IRS spectra of a $z = 0.7$ sample to estimate the SF and AGN contribution to LF. In Figure 11, we compare the 15 μm SF LF (red diamonds) from 5MUSES with the corresponding 15 μm SF LF at $z = 0.7$ by Fu et al. (2010, blue squares). In the same figure, we also overplot the total 15 μm LF derived from the 5MUSES sample (black filled circles) and its counterpart at $z = 0.7$ from the work of Le Floc'h et al. (2005, yellow crosses). We observe strong evolution

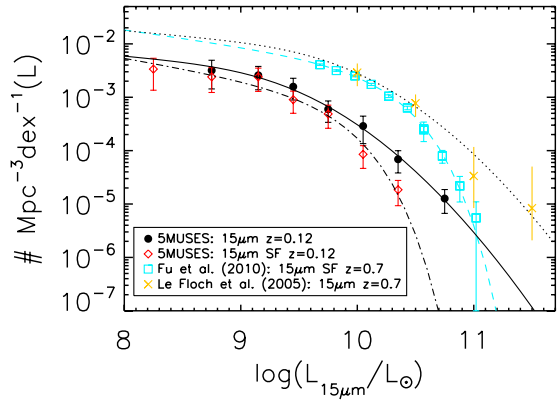

Figure 11. Comparison of LF at $\langle z \rangle = 0.12$ from our sample with LFs at $\langle z \rangle = 0.7$. The black filled circles represent the total 15 μm LF and the red open diamonds represent the 15 μm SF LF derived from our sample. The black dash-dotted line and the solid line are the best fits to the SF LF and total LF derived from the 5MUSES sample at 15 μm, respectively. The blue open squares represent the 15 μm SF LF at $z = 0.7$ from Fu et al. (2010) and the yellow crosses represent the total 15 μm LF from Le Floc'h et al. (2005). The blue dashed line is the best-fit Schechter function from Fu et al. (2010) to the 15 μm SF LF at $z = 0.7$. The black dotted line is derived by evolving the luminosity and density of LFs from 5MUSES by a factor of $\alpha_L = 2.6$ and $\alpha_D = 2.1$ (Le Floc'h et al. 2005) and it appears to match well with the 15 μm LF at $z = 0.7$ by Le Floc'h et al. (2005).

(A color version of this figure is available in the online journal.)

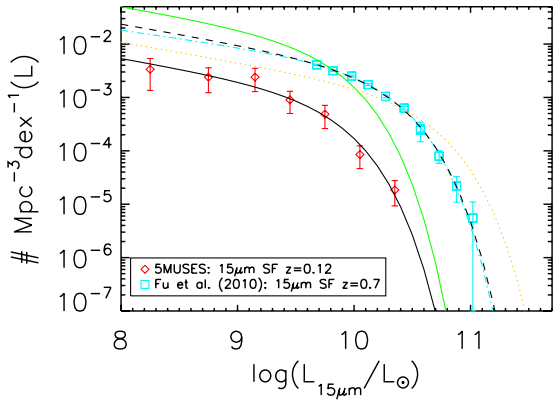

Figure 12. Comparison of the 15 μm SF LF from 5MUSES (red diamonds) at $\langle z \rangle = 0.12$ and from Fu et al. (2010, blue squares) at $\langle z \rangle = 0.7$. The black solid line and the blue dash-dotted lines are the best fits to the two LFs, respectively. The green dash-dot-dot line represents the best fit when only evolution on density is allowed ($\alpha_D = 5.3$). The yellow dotted line represents the best fit when only evolution on luminosity is allowed ($\alpha_L = 4.3$). The black dashed line represents the best fit when both density and luminosity evolution are allowed ($\alpha_D = 2.5$, $\alpha_L = 2.6$).

(A color version of this figure is available in the online journal.)

effects in both the total and the SF LFs. With data only in two redshift bins ($z = 0.12$ and $z = 0.7$), we were not able to place stringent constraints on the amount of evolution on density (α_D) and luminosity (α_L), however, if we adopt the values proposed by Le Floc'h et al. (2005) and evolve our total 15 μm LF at $z = 0.12$ to $z = 0.7$ by a factor of $\alpha_D = 2.1$ and $\alpha_L = 2.6$, we find a good match between the evolved LF (black dotted line) and the observed data (yellow crosses).

We follow a similar approach to evolve the 15 μm SF LF from $z = 0.12$ to $z = 0.7$. In Figure 12, we show that if we evolve our 15 μm SF LF at $z = 0.12$ (black solid line) by a factor of $\alpha_D = 2.5$ and $\alpha_L = 2.6$, it matches very well (reduced $\chi^2 = 0.6$) with the observed rest-frame 15 μm SF LF at $z = 0.7$ from Fu et al.'s (2010) work (blue dashed line). Could a pure density evolution or luminosity evolution explain the difference we observe in the SF LF at $z = 0.12$ and $z = 0.7$? In Figure 12, we show the best fit to the SF LF at $z = 0.7$ if we only allow density evolution on our local SF LF (green dash-dot-dot line). The best fit returns $\alpha_D = 5.3$ and the reduced $\chi^2 = 65.6$. In the same figure, we also show the best fit when only luminosity evolution is allowed (yellow dotted line). We find $\alpha_L = 4.3$ and the reduced $\chi^2 = 70.0$. Even though we only have data in two redshift bins, which makes it difficult to place stringent constraints on the amount of evolution we require on luminosity and density, we can at least confirm from our work that neither pure luminosity nor pure density evolution is sufficient to explain the difference between SF LFs at $z = 0.12$ and $z = 0.7$.

We should however point out some caveats. Although both our work and Fu et al.'s (2010) work used IRS spectra as diagnostic tools for distinguishing between SF and AGN, our LF is derived by separating the energy density contribution in each source, while they use IRS spectra to determine the major source of energy in each object, and then remove the AGN-dominated sources when building their SF LF. Because they only have IRS spectra for ~40 galaxies from their flux-limited sample, the low end of their SF LF is obtained by shifting the MIPS 24 μm luminosity to rest-frame 15 μm ($z = 0.7$), and they assign these low-luminosity objects as dominated by SF. Given our very rigorous analysis, we clearly see some differences in the total LF and the SF LF at 15 μm even at the low-luminosity end (see the comparison of the black dot-dashed line and the black solid line), thus Fu et al. (2010) might have overestimated the SF LF below $L_{15\,\mu m} = 10^{10.5}\,L_\odot$.

5. CONCLUSIONS

We have analyzed a *Spitzer* spectroscopic sample of 24 μm selected objects in the SWIRE and XFLS fields to derive the 15 and 24 μm LFs at $0 < z < 0.3$. When combined with local and high-redshift studies, this provides critical information on understanding the evolution of energy budgets over the past three billion years ($z < 0.3$). Our conclusions are summarized as follows.

1. We have derived 24 and 15 μm LFs for our sample at $z < 0.3$. The availability of the 5–35 μm allows us to make *k*-corrections directly using the observed SED. The 24 and 15 μm LFs display rather shallow slopes at the bright end, which is due to the increase of AGN contribution in more luminous systems.
2. Using the 5–35 μm IRS spectra, we have decomposed the 5MUSES objects into SF and AGN components. The SF fraction is taken to be the median likelihood of the pdf. We calculate the 15 and 24 μm SF luminosities in each object, and subsequently build the SF LFs. The SF LFs can be described with a Schechter function.
3. We have also estimated the SF contribution to the integrated 15 and 24 μm luminosity density for our sample. The SF fraction is found to be 58% at 15 μm and goes up to 78% at 24 μm. Using the conversion factor from L_{MIR} to L_{IR} for star-forming galaxies and AGNs, respectively, we found the SF fraction to be ~86% in the total IR luminosity density.
4. The SF fraction is also found to be a function of luminosity/redshift, decreasing as luminosity or redshift increases, while the trend is more obvious in mid-IR, suggesting that the mid-IR wavelength is more sensitive to the presence of AGNs.
5. Both luminosity and density evolution are required to explain the difference in the observed SF LF between this sample and similar studies at $z \sim 0.7$.

We thank J.-S. Huang, V. Charmandaris, H. Fu, and E. Le Floc'h for insightful discussion. This work was based on observations made with the *Spitzer Space Telescope*, which is operated by JPL/Caltech under a contract with NASA. The observations are associated with the *Spitzer* Legacy Program 40539. The authors acknowledge support by NASA through awards issued by JPL/Caltech. This research has made use of the NASA/IPAC Extragalactic Database (NED) which is operated by the Jet Propulsion Laboratory, California Institute of Technology, under contract with the National Aeronautics and Space Administration.

REFERENCES

Armus, L., et al. 2007, ApJ, 656, 148
Armus, L., et al. 2009, PASP, 121, 559
Arnouts, S., et al. 2005, ApJ, 619, L43
Bothwell, M. S., et al. 2011, MNRAS, in press
Caputi, K. I., et al. 2007, ApJ, 660, 97
Chary, R., & Elbaz, D. 2001, ApJ, 556, 562
Dey, A., et al. 2008, ApJ, 677, 943
Elbaz, D., et al. 1999, A&A, 351, L37
Fu, H., et al. 2010, ApJ, 722, 653
Goto, T., et al. 2011, MNRAS, 410, 573
Hopkins, A. M., & Beacom, J. F. 2006, ApJ, 651, 142

Hopkins, P. F., Richards, G. T., & Hernquist, L. 2007, ApJ, 654, 731
Hopkins, P. F., Younger, J. D., Hayward, C. C., Narayanan, D., & Hernquist, L. 2010, MNRAS, 402, 1693
Houck, J. R., et al. 2004, ApJS, 154, 18
Houck, J. R., et al. 2005, ApJ, 622, L105
Huang, J.-S., et al. 2007, ApJ, 664, 840
Ilbert, O., et al. 2005, A&A, 439, 863
Kennicutt, R. C., Jr., et al. 2003, PASP, 115, 928
Le Floc'h, E., et al. 2005, ApJ, 632, 169
Lilly, S. J., Le Fevre, O., Hammer, F., & Crampton, D. 1996, ApJ, 460, L1
Madau, P., Ferguson, H. C., Dickinson, M. E., Giavalisco, M., Steidel, C. C., & Fruchter, A. 1996, MNRAS, 283, 1388
Magnelli, B., Elbaz, D., Chary, R. R., Dickinson, M., Le Borgne, D., Frayer, D. T., & Willmer, C. N. A. 2009, A&A, 496, 57
Matute, I., La Franca, F., Pozzi, F., Gruppioni, C., Lari, C., & Zamorani, G. 2006, A&A, 451, 443
Menéndez-Delmestre, K., et al. 2009, ApJ, 699, 667
Murphy, E. J., Chary, R.-R., Alexander, D. M., Dickinson, M., Magnelli, B., Morrison, G., Pope, A., & Teplitz, H. I. 2009, ApJ, 698, 1380
Nardini, E., Risaliti, G., Salvati, M., Sani, E., Imanishi, M., Marconi, A., & Maiolino, R. 2008, MNRAS, 385, L130
Oliver, S. J., et al. 2010, A&A, 518, L21
Papovich, C., et al. 2006, AJ, 132, 231
Pérez-González, P. G., et al. 2005, ApJ, 630, 82
Petric, A., et al. 2011, ApJ, 730, 28
Pope, A., et al. 2008, ApJ, 675, 1171
Pozzi, F., et al. 2004, ApJ, 609, 122
Reddy, N. A., Steidel, C. C., Pettini, M., Adelberger, K. L., Shapley, A. E., Erb, D. K., & Dickinson, M. 2008, ApJS, 175, 48
Rieke, G. H., & Low, F. J. 1972, ApJ, 176, L95
Rieke, G. H., et al. 2004, ApJS, 154, 25
Rujopakarn, W., et al. 2010, ApJ, 718, 1171
Rush, B., Malkan, M. A., & Spinoglio, L. 1993, ApJS, 89, 1
Sajina, A., et al. 2008, ApJ, 683, 659
Sanders, D. B., Mazzarella, J. M., Kim, D.-C., Surace, J. A., & Soifer, B. T. 2003, AJ, 126, 1607
Saunders, W., Rowan-Robinson, M., Lawrence, A., Efstathiou, G., Kaiser, N., Ellis, R. S., & Frenk, C. S. 1990, MNRAS, 242, 318
Schechter, P. 1976, ApJ, 203, 297
Schmidt, M. 1968, ApJ, 151, 393
Shupe, D. L., Fang, F., Hacking, P. B., & Huchra, J. P. 1998, ApJ, 501, 597
Soifer, B. T., Sanders, D. B., Madore, B. F., Neugebauer, G., Danielson, G. E., Elias, J. H., Lonsdale, C. J., & Rice, W. L. 1987, ApJ, 320, 238
Veilleux, S., et al. 2009, ApJS, 182, 628
Werner, M. W., et al. 2004, ApJS, 154, 1
Wu, Y., et al. 2010, ApJ, 723, 895
Xu, C. 2000, ApJ, 541, 134
Yan, L., et al. 2007, ApJ, 658, 778
Yuan, T.-T., Kewley, L. J., & Sanders, D. B. 2010, ApJ, 709, 884